Science Advances
AAAS

advances.sciencemag.org/cgi/content/full/6/13/eaaz2598/DC1

Supplementary Materials for

Biomimetic human small muscular pulmonary arteries

Qianru Jin, Anil Bhatta, Jayson V. Pagaduan, Xing Chen, Hoku West-Foyle, Jiayu Liu, Annie Hou, Dan Berkowitz, Scot C. Kuo, Frederic B. Askin, Thao D. Nguyen, David H. Gracias*, Lewis H. Romer*

*Corresponding author. Email: dgracias@jhu.edu (D.H.G.); lromer@jhmi.edu (L.R.)

Published 25 March 2020, *Sci. Adv.* **6**, eaaz2598 (2020)
DOI: 10.1126/sciadv.aaz2598

The PDF file includes:

Other Supplementary Material for this manuscript includes the following:

(available at advances.sciencemag.org/cgi/content/full/6/13/eaaz2598/DC1)

I. Supplementary Figures

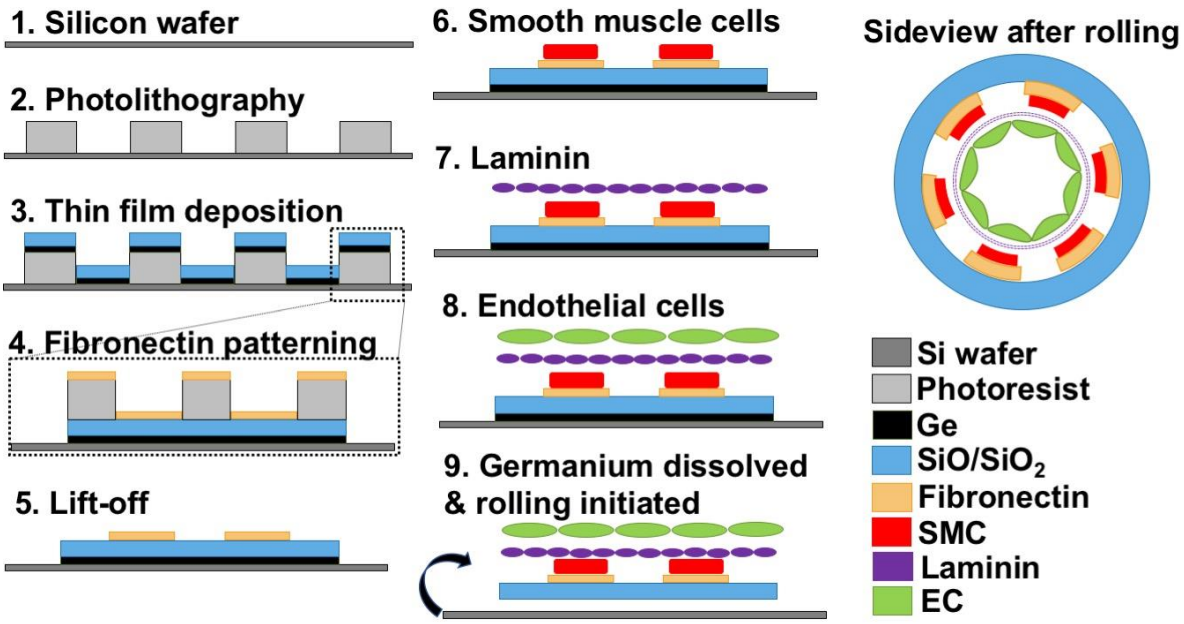

Fig. S1. A schematic illustration of detailed fabrication process. The fabrication process requires two patterning steps which were achieved using photolithography, followed by cell and laminin deposition and dissolution of the sacrificial layer to trigger self-rolling of the tubes. **Parts 1-3:** The first patterning step was used to define circular discs of germanium (Ge), silicon monoxide (SiO) and silicon dioxide (SiO2). These round discs will eventually roll up into the tubes. It is noteworthy that the size and/or shapes of these 2D precursors can be modulated to vary diameter and rolling characteristics. The schematics illustrate this process which includes (1) cleaning silicon wafer substrates, (2) patterning photoresist, and 3) sequential addition of Ge, SiO and SiO2 by physical vapor deposition. After dissolution of the photoresist, only the discs remain on the Si wafer substrate. **Parts 4-5:** The second patterning step was used to create fibronectin lines on the discs to align smooth muscle cell adhesion and growth. The schematics illustrate this process which includes (4) photoresist patterning to create linear patches followed by fibronectin deposition, and (5) lift-off of the photoresist by dissolution. This step results in the definition of circular discs of Ge/SiO/SiO2 with linear patterns of fibronectin on them. **Parts 6-8:** The biological components of the arteries are then deposited as shown in the schematics and this includes (6) seeding smooth muscle cells (SMC) which adhere to the fibronectin patterned lines causing them to be aligned, (7) laminin layering on top of the SMC, and (8) seeding endothelial cells (EC) on top of the laminin. Finally, (9) the Ge layer dissolves following approximately 10h of exposure to aqueous cell culture medium and self-rolling occurs. The side view shows the tubular construct with layers of patterned fibronectin, patterned smooth muscle cells, laminin and endothelial cells. A color key is provided at the lower right.

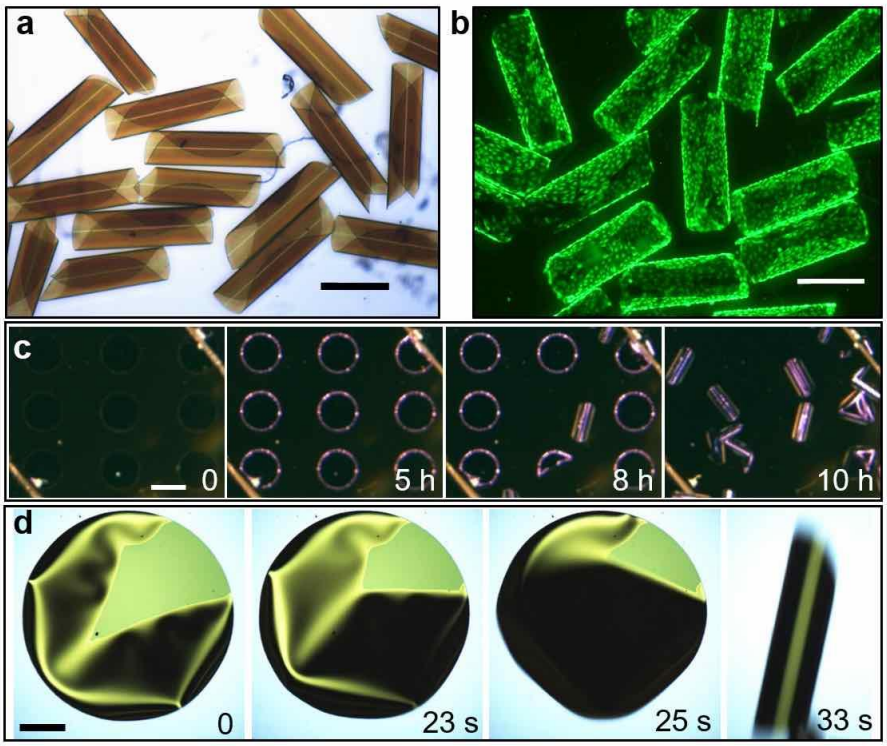

Fig. S2. Self-folding of silicon monoxide and silicon dioxide bilayer films. (**A**) Brightfield images of tubular constructs (1mm in length) after release and folding, demonstrating the transparency of the films. Scale bar = 500 µm. (**B**) Epifluorescence images of live endothelial cells growing on the luminal side of the tubular constructs, stained with Calcein-AM. Scale bar = 500 µm. (**C**) A time series of brightfield images demonstrated the roll-up process over 10 hours from treating with 37 ºC PBS until all films rolled up. Scale bar = 1mm. (**D**) A time series of brightfield snapshots of shape changes during the terminal roll-up process in which the circular thin film rolls into a tube. Scale bar = 200 µm.

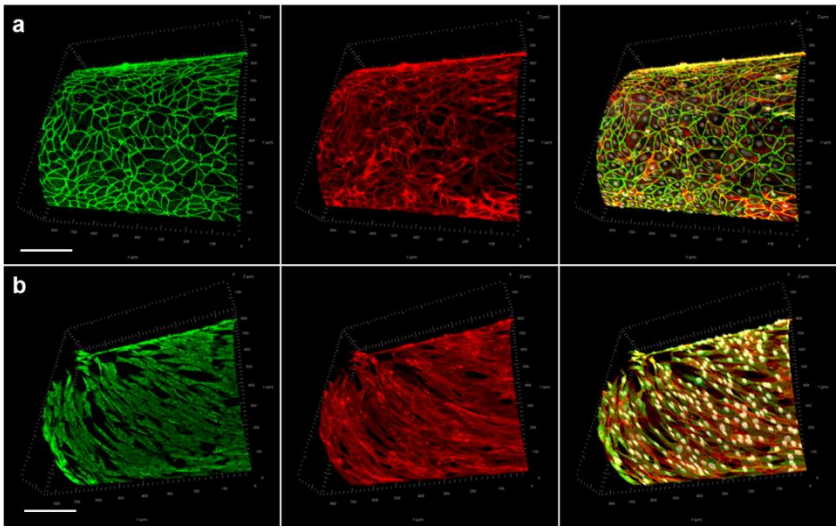

Fig. S3. ECs and SMCs form a monolayer in biomimetic microvessels. (**A**) Confocal microscopy images of human pulmonary microvascular endothelial cells (HPMEC) showing VE-cadherin (green), F-actin (red) and nuclei (grayscale). Cells were grown on the luminal surface of the tube. One quarter of the tube is shown. Scale bar = 200 µm. (**B**) Confocal microscopy images of human pulmonary artery smooth muscle cells (HPASMC) showing smooth muscle α-actin (green), F-actin (red) and nuclei (grayscale). Cells were grown on the luminal surface of the tube. One quarter of the tube is shown. Scale bar = 200 µm.

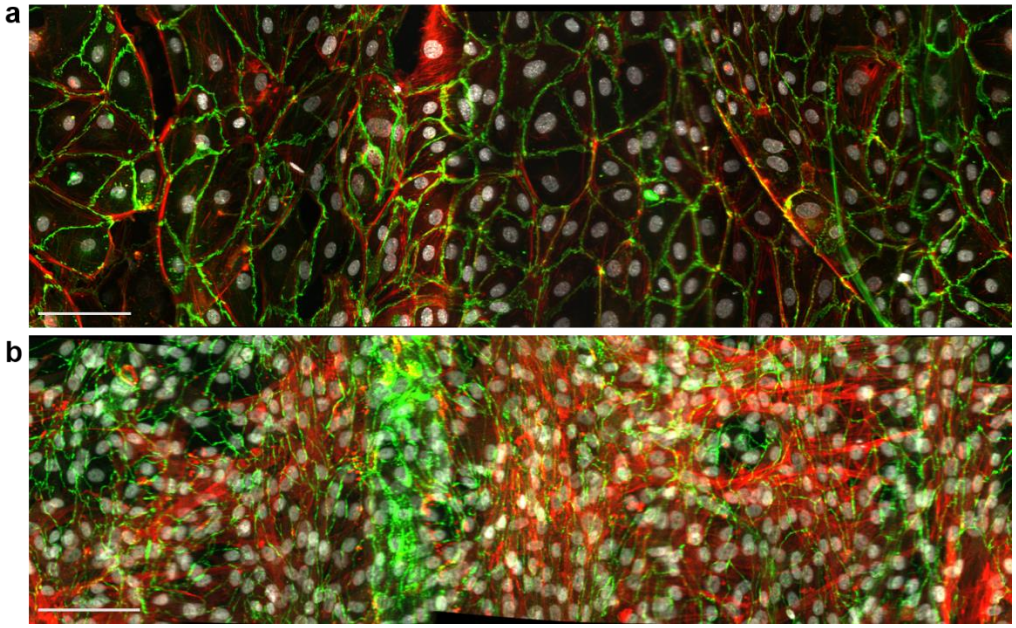

Fig. S4. Cells on the luminal surface of the tube (digitally unrolled). Confocal microscopy images of (**A**) HPMEC showing endothelial transmembrane junction protein VE-cadherin (green), F-actin (red) and nuclei (grayscale); (**B**) co-cultures of HPMEC and HPASMC, showing the endothelial adherens junction protein VE-cadherin between HPMEC (green), smooth muscle α-actin of HPASMC (red) and nuclei of both cell types (grayscale). Images are stitched from 4 digitally unrolled z-stacks acquired at 90-degree intervals around the axis of the tube. The stitched image shows complete cell coverage of the luminal surface of the tube. Scale bars = 100 µm.

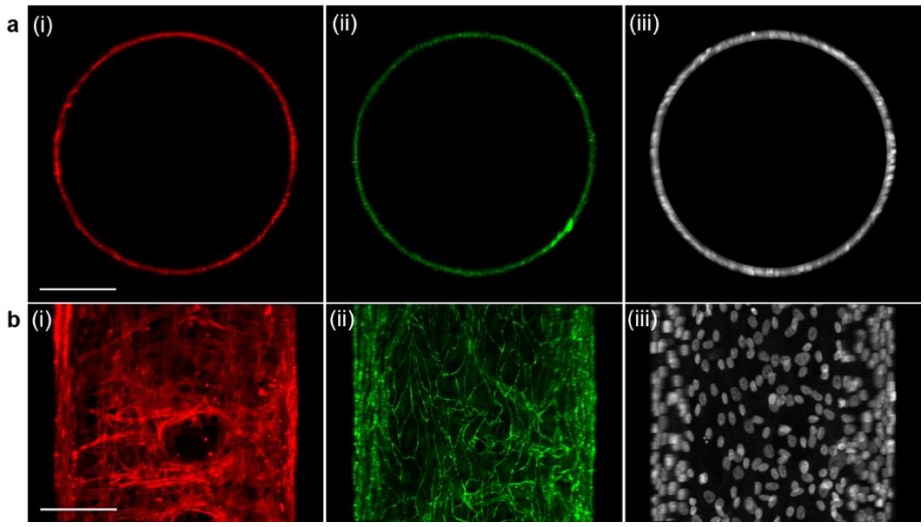

Fig. S5. Biomimetic microvessel populated by cocultured HPMEC and HPASMC, cross-sectional and en face views. Confocal microscopy images of co-cultures of HPMEC and HPASMC, VE-cadherin of HPMEC (green), smooth muscle α-actin of HPASMC (red) and nuclei of both cell types (grayscale), displayed in two projections: (**A**) cross-sectional view, and (**B**) *en face* view. Scale bars = 100 µm.

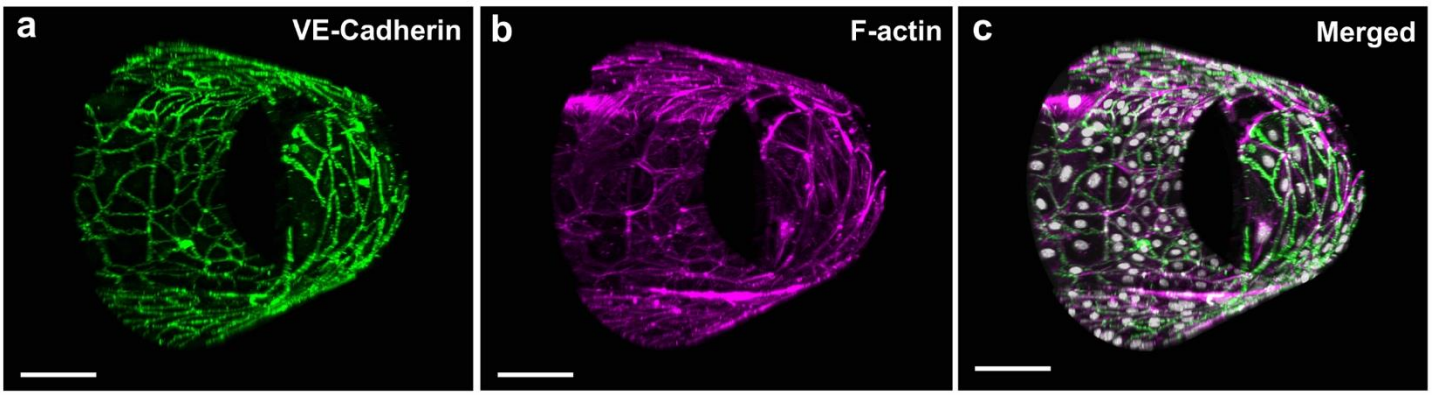

Fig. S6. Green-magenta version of data in Fig. 3: 3D reconstructions of biomimetic microvessels with ECs illustrating uniformity of cell coverage and intercellular junctional morphology. Reconstructions of confocal z-stacks of biomimetic microvessels populated by human pulmonary microvascular endothelial cells (HPMECs), featuring: (**A**) VE-cadherin at endothelial adherens junctions (antibody labeling, green), (**B**) F-actin (phalloidin, magenta) and (**C**) merged images that include nuclei (DAPI, grayscale). Insets in (A) and (B) show the cross-sectional views of the tube in the corresponding color channel and demonstrate the amount of overlap due to the roll up process. Scale bars = 100 µm.

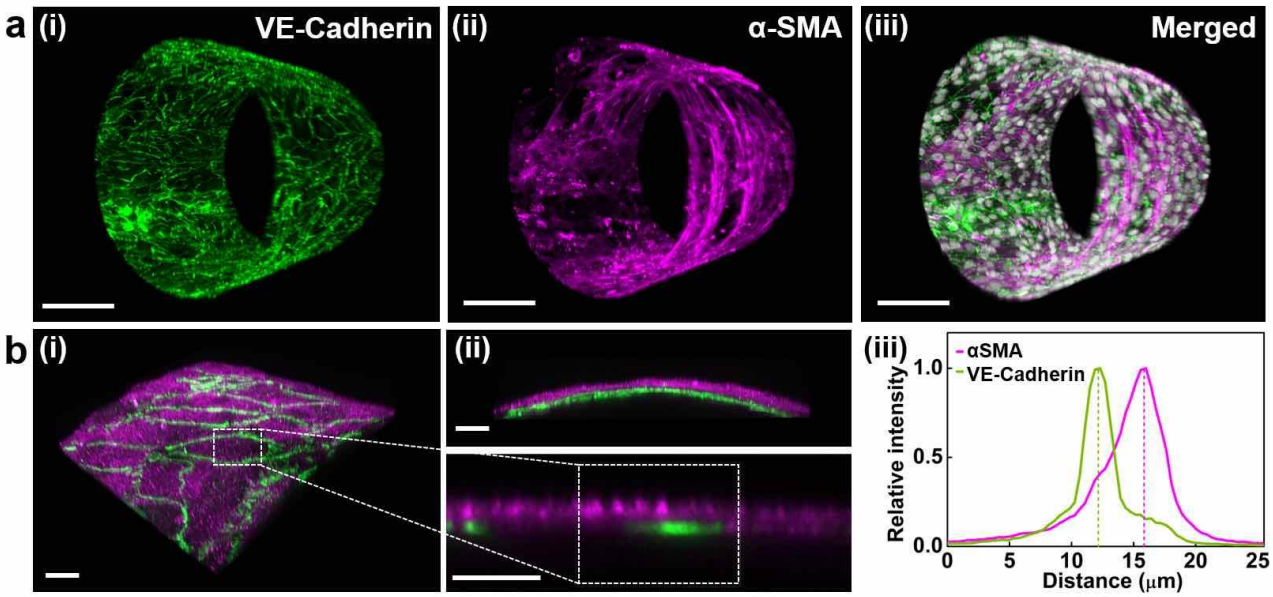

Fig. S7. Green-magenta version of data in Fig. 4: HPMECs and HPASMCs are layered in biomimetic hSMPA. (**A**) Reconstructions of confocal z-stacks of biomimetic hSMPA populated by layered co-cultures of HPMEC (luminal) and HPASMC. (i) VE-cadherin (antibody labeling, green), (ii) smooth muscle α-actin (antibody labeling, magenta), (iii) merged image including nuclei from both cell types (DAPI, grayscale). Scale bars = 100 μm. (**B**) (i) 3D view of two-channel confocal imaging of a small region of a biomimetic hSMPA. HPMECs are visualized using anti-VE-cadherin antibody (green), while smooth muscle α-actin antibody labeling (magenta) shows the HPASMC. (ii) XZ projection demonstrates segregation and layering of these two cellular components in this biomimetic hSMPA. The lower panel in (ii) is sampled from (i) and exhibits intensity distribution. Scale bars = 20 μm. (iii) Normalized fluorescence intensity is plotted vs. relative radial distance from the tube's lumen. The distance between the two cell layers is approximately 3.5 μm.

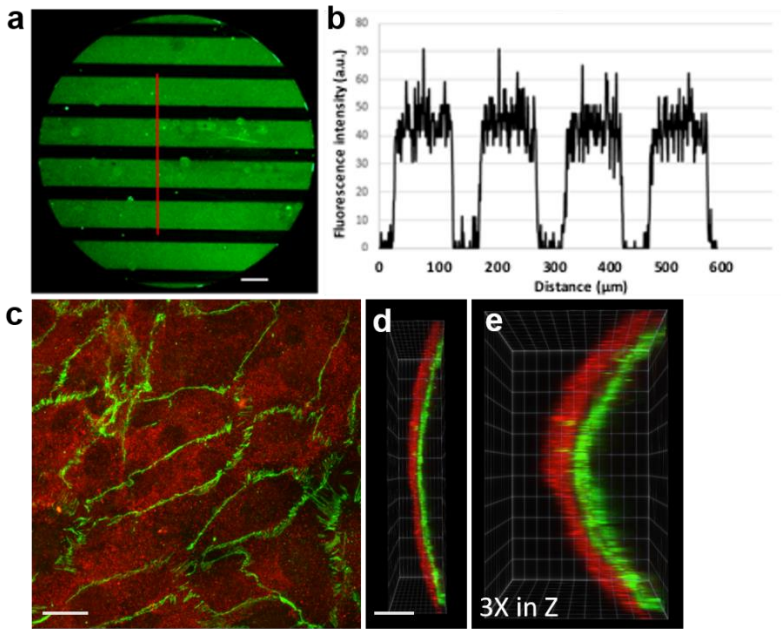

Fig. S8. SMC patterning and layering of multiple cell types. (**A**) Surface can be selectively modified to guide cell alignment using photolithography. FITC-labeled BSA was selectively adsorbed and fluorescence intensity was measured to test the quality of protein patterning. Scale bar = 50 µm. (**B**) Graph shows fluorescence intensity as an indicator of protein adsorption along the linear path indicated by the red line. For cell culture, surfaces were modified with unlabeled fibronectin. (**C**)Maximum intensity projection of confocal microscopy images of co-cultures of HPMECs and HPASMCs in biomimetic hSMPA, showing VE-cadherin of HPMECs (green), and smooth muscle α-actin of HPASMCs (red). Scale bar = 20 µm. (**D**)Side view shows layering of the two cell types. Scale bar = 20 µm. (**E**)Same field as (B), with z-dimension enlarged 3-fold to highlight layering.

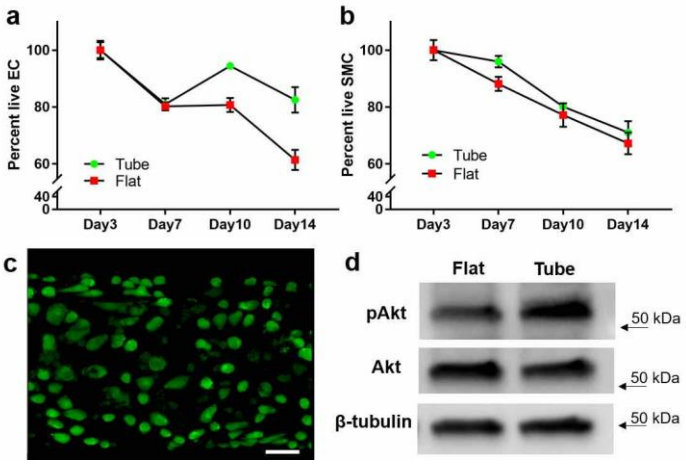

Fig. S9. Cell longevity and HPMEC function studies. (**A**-**B**) Cell viability was calculated as the percentage of live cells compared with baseline (day 3) using the CyQUANT assay. HPMEC (A) and HPASMC (B) populations were assayed. HPMEC cells show improved longevity in tubular constructs compared to those on flat substrate. Data from flat (red) and tubular constructs (green) were compared. (**C**) Confocal microscopy image showing nitric oxide production as indicated by DAF-2 DA (diacetate, 10 μmol/L, 30 minutes) fluorescence from HPMEC in a biomimetic microvessel. Scale bar = 50 μm. (**D**) An example western blot of phospho-Akt (pThr308), total Akt and β-tubulin as a loading control. Experiments were repeated five times and the ratios obtained by densitometry for Akt phosphorylation in tubular constructs divided by flat cultures were as follows: 1.40:1, 0.89:1, 0.40:1, 1.59:1, 2.35:1. Three out of five experiments showed increased pAkt in HPMECs cultivated in tubular constructs as compared with pAkt levels in their counterparts that were cultivated on flat constructs.

II. Supplementary Methods

II.1 Image processing

All images for 3D tube presentation were processed by the following steps.
1) Image stacks were obtained from each of the 4 sides of the rectangular capillary. Each stack was processed individually first.

The stack was first corrected for axial chromatic aberrations using measured offsets, and then resampled to achieve isotropic voxels. This ensured that there was no loss of resolution upon further transformations. The stack was then rotated by 90 degrees in the Y direction to allow automated measurement of the arc of the tube through the entire stack. These measurements were then used to calculate rotation corrections to align the tube orthogonally to the reference frame.

The stack was then straightened in ImageJ. A polyline was drawn manually along the arc of the aligned tube. The ‘Straighten’ function in ImageJ digitally “unwrapped” this curved surface and generated a thin Z-stack, analogous to a cartographic projection. These 4 thin Z-stacks were then automatically stitched in ImageJ, using the DAPI channel as a reference due to its consistency across cell types and stains. The end result was a digitally unrolled cylinder of consistent image quality across its extent. This data could be analyzed directly, or projected back to a cylindrical surface for visualization purposes by employing a Matlab script.

2) The final stitched image was loaded in Matlab, and its size was used to determine the diameter and length of a cylinder. Next, the coordinates of each voxel in this cylinder were mapped to its corresponding coordinates in the stitched image. Voxel values were then calculated by summing the values of six overlapping voxels, that were weighted by distance. The resulting 3D image was then exported, and visualized in Imaris.

II.2 Finite Element Simulation

Analytical scaling law of thin-walled circular cylinder subjected to concentrated radial loads

In this study, we demonstrated the ability to culture cells on thin structures composed of SiO and SiO_2, which have an elastic Young's modulus that is six orders of magnitude larger than the modulus of the extracellular matrix material of the human arteriole. Thin films of SiO and SiO_2 were induced to fold into a cylindrical tube by the fabrication process and left free-floating in the cell culture media. To investigate the ability of cells cultured on the surface to deform the tube, we considered a simplified model of a thin-walled cylindrical shell loaded by two concentrated, diametrically opposed, radial forces, as shown in Figure 2a (left panel).

Semi-analytical solutions have been developed for the radial displacement w_0 under the radial load by classical shell theory,(*36*) which assumes small deflection, linear elastic, isotropic, homogeneous properties, as incorporated into Equation 1 (Eq1) below

$$\left(\frac{R}{t}\right)\left(\frac{Et^2}{F}\right)\frac{w_0}{R}=\frac{K}{2\pi}+\frac{2K}{\pi}\sum_{n=2,4,\ldots}^{m-2}\left\{1+\frac{2K^2n^2}{\left(n^2-1\right)\left(2n^2-1\right)}\right\}+\frac{K^4\sqrt{2}}{\pi}\sum_{n=m,m+2,\ldots}^{\infty}\left\{\frac{\left(K_n+1\right)^{1/2}}{n^3K_n}\right\} \quad \text{(Eq1)}$$

where R and t are the radius and wall thickness of the thin-walled cylinder; E and ν are the Young's modulus and Poisson's ratio; F is the concentrated radial load; K is the non-dimensional structural parameter defined by Equation 2 (Eq2) below

$$K^4=3\left(1-\nu^2\right)\left(\frac{R}{t}\right)^2 \quad \text{(Eq2)}$$

The n is an even integer; K_n is defined by $1+K^4/n^4$; and m is the first even integer satisfying

$$5m^2\left(2m^2-1\right)^2>16K^4 \quad \text{(Eq3)}$$

For a thin-walled cylindrical shell ($\frac{R}{t}>100$) of incompressible material, m = 6 is the first even integer that satisfies Eq3. Plugging into Eq1, gives Equation 4 (Eq4) below

$$\left(\frac{R}{t}\right)\left(\frac{Et^2}{F}\right)\frac{w_0}{R}=\frac{K}{2\pi}+\frac{2K}{\pi}\left(2+\frac{488}{1085}K^2\right)+\frac{K^4\sqrt{2}}{\pi}\sum_{n=6,8,\ldots}^{\infty}\left\{\frac{\left(2+\frac{K^4}{n^4}\right)^{1/2}}{n^3\left(1+\frac{K^4}{n^4}\right)}\right\} \quad \text{(Eq4)}$$

For the infinite series in Eq4, we only considered the first term with n = 6, which is the largest term in the series, and omit the higher *n* terms

$$\left(\frac{R}{t}\right)\left(\frac{Et^2}{F}\right)\frac{w_0}{R}=\frac{9K}{2\pi}+\frac{976}{1085\pi}K^3+\frac{K^4\sqrt{2}}{\pi}\left\{\frac{\left(2+\frac{K^4}{1296}\right)^{1/2}}{216\left(1+\frac{K^4}{1296}\right)}\right\} \quad \text{(Eq5)}$$

The K is large for thin-walled shell, and neglecting the lower order terms of *K* gives

$$\frac{w_0}{R}=\frac{976}{1085\pi}K^3\left(\frac{F}{Et^2}\right)\left(\frac{t}{R}\right) \quad \text{(Eq6)}$$

Substituting Eq2 into Eq6, we obtained the analytical scaling law of the problem as

$$w_0 = C\frac{FR^{\frac{3}{2}}}{Et^{\frac{5}{2}}} \quad \text{(Eq7)}$$

where $C=\frac{976}{1085\pi}\left\{3\left(1-\nu^2\right)\right\}^{3/4}$ is a proportionality constant, which equals 0.5269 for incompressible material.

The stiffness of the tube can be identified as

$$\psi=\frac{Et^{\frac{5}{2}}}{CR^{\frac{3}{2}}} \quad \text{(Eq8)}$$

In a later work,(*37*) S.A. Łukasiewicz evaluated the theoretical model obtained in the reference (*36*) using different numerical approximations and found *C* = 0.74. In the same work, the author also derived from the Donnell-Vlasov theory of shell, which assumed short wavelength deformations, and found the same scaling law for w_0 but with a smaller proportionality constant, *C* = 0.555.

Finite element analysis of thin-walled circular cylinder subjected to concentrated radial loads

We applied finite element analysis (FEA) to verify the analytical scaling law and obtain the proportionality constant *C* in Eq7. We used Abaqus 6.14 (Dassault Systèmes Simulia Corp, Providence, RI, USA) to develop finite element models of a thin-walled SiO cylindrical shell with a length of L = 1 mm, a radius of R = 125 μm and different wall thicknesses (t = 1.2 μm, 1.4 μm, 1.6 μm, 1.8 μm, or 2 μm) subjected to equal and opposite concentrated radial loads (F = 2.432 μN, 4.4 μN, 8.8 μN, or 13.2 μN) applied by the cell.(*39*)

A generalized Hooke's law was used to describe the mechanical properties of SiO with Young's modulus E = 77 GPa and Poisson's ratio ν = 0.2. The concentrated radial loads were simulated by a pressure (P) applied on a small area (S) (Figure S10a). In the reference, (*39*) the cross-sectional area of a single smooth muscle cell is 12.6 μm^2, which corresponds to a circle of diameter 4 μm. For simplicity, the loading area in the model was chosen to be a square of edge length 4 μm. The pressures applied were 0.152 MPa, 0.275 MPa, 0.55 MPa, or 0.825 MPa. The displacement boundary conditions were set as

$$\begin{aligned} u_x(x=0,y,z) &= \theta_y(x=0,y,z) = \theta_z(x=0,y,z) = 0 \\ u_y(x,y=0,z) &= \theta_x(x,y=0,z) = \theta_z(x,y=0,z) = 0 \\ u_z(x,y,z=0) &= \theta_x(x,y,z=0) = \theta_y(x,y,z=0) = 0 \end{aligned} \qquad \text{(Eq9)}$$

where u_x, u_y and u_z are the displacement along x, y and z axis; θ_x, θ_y and θ_z are the rotational displacement about x, y and z axis.

Considering the symmetry in X, Y and Z directions of the problem, only 1/8 of the thin-walled tube was used by the model. The mesh was discretized using S4R elements (4-node, quadrilateral, doubly curved thin or thick shell with reduced integration) and a higher mesh density was chosen at the loading region. In total, the simulations considered 5 different shell thicknesses, and 4 different pressure loads for each thickness value. We performed a mesh convergence study for all 20 cases to verify the mesh-independence of the results.

Figure S10b shows the deformed shape of the tube of wall thickness 1.2 μm (magnified by a factor of 500) for an applied force F = 13.2 μN. Plots of the radial displacement w0 as a function of $FR^{\frac{3}{2}} / Et^{\frac{5}{2}}$. for all 20 cases exhibited a linear relationship (Figure S10c) as expected from the analytically derived scaling law in Eq7. A linear regression of the w0 as a function of $FR^{\frac{3}{2}} / Et^{\frac{5}{2}}$. gave C = 1.173 for the proportionality constant.

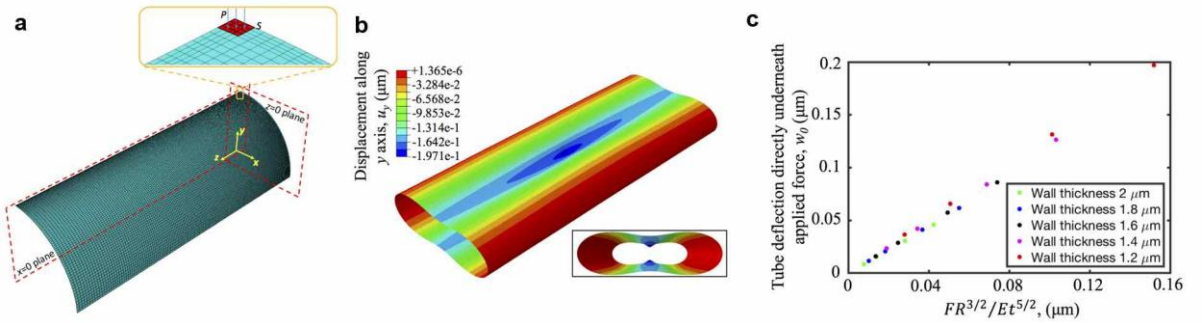

Fig. S10. Finite element study details. (**A**) Finite element model of the thin-walled cylindrical shell. $x = 0$ plane and $z = 0$ plane are shown to help with the visualization. (**B**) Contour plot of the displacement along y axis of the deformed configuration. The front view of the deformed cylindrical shell is shown in the inset. A magnification factor of 500 is used to help with the visualization. (**C**) The deflection of tube directly underneath the applied force, obtained by finite element analysis for all 20 cases, was plotted against $FR^{\frac{3}{2}} / Et^{\frac{5}{2}}$.

Movie S1. Video for 3D view of hSMPA populated by HPMECs.

Movie S2. Video for 3D view of hSMPA populated by coculture of HPMECs and HPASMCs.